Batteries & Supercaps

Research Article
doi.org/10.1002/batt.202200116

Chemistry Europe
European Chemical Societies Publishing

www.batteries-supercaps.org

Experimentally Validated Three-Dimensional Modeling of Organic-Based Sodium-Ion Battery Electrode Manufacturing

Teo Lombardo[+,[a, b]] Fanny Lambert[+,[a, b, c]] Roberto Russo[+,[a, b, d]] Franco M. Zanotto,[a, b] Christine Frayret,[a, b, e] Gwenaelle Toussaint,[b, d] Philippe Stevens,[b, d] Matthieu Becuwe,[a, b] and Alejandro A. Franco*[a, b, e, f]

Lithium-ion batteries (LIBs) have triggered the transition from internal combustion engine cars to electric vehicles, and are also making inroads into the grid storage sector, but the future quantity of batteries necessary poses several challenges in terms of raw material availability and sustainability. For this reason, many alternative chemistries are being proposed, such as substituting lithium with other more abundant elements, like sodium, or shifting from inorganic to organic-based active materials, all of which require the development and testing of new chemistries. The electrode properties are not only a function of the chemistry, but also of the electrode manufacturing and resulting microstructure. In this work, we applied a three-dimensional computational workflow, initially developed in the context of inorganic-based electrodes for LIBs, to simulate the manufacturing of sodium-ion battery anodes using an in-house synthesized organic-based active material. This computational workflow accounts for the slurry, its drying, and electrode calendering steps, and was validated by comparing simulated and experimental properties of the slurry and electrode. In addition, the calendering step was studied computationally to identify optimal electrode compressions, and the trend observed was confirmed experimentally through galvanostatic cycling in half-cell configuration. The positive results shown here are an important demonstration of the chemistry neutrality of our manufacturing models, paving the way towards their application to both commercial and novel chemistries.

Introduction

Batteries in general, and lithium-ion batteries (LIBs) in particular, are key technologies of our time, widely used in portable electronics, and the current state of the art for electric vehicles (EVs) applications. Nevertheless, current LIBs and their production upscale face a series of key challenges, like the use of non-abundant and expensive inorganic materials based on Lithium, Cobalt, or Nickel, among others,[1,2] which can lead to supply chain risks and higher costs.[3–6] Furthermore, recent directives impose new environmental requirements, like the European 2006/66/EC directive that aims to minimize the negative environmental impacts of battery production and waste.[7]

To overcome these problems and meet these new directives, eco-designed organic-based materials for energy storage applications look promising as alternative materials for the next generation of monovalent (Li^+, Na^+, K^+, etc.), or di- and trivalent (Mg^{2+}, Al^{3+}, Ca^{2+}, etc.) ion-based batteries.[8] These alternative chemistries will likely not substitute entirely inorganic-based LIBs but could be complementary to them, for instance for power applications or to relieve partially the pressure on the battery supply chains. Organic electrodes can bring several environmental advantages: they are made of naturally abundant materials (e.g., C, H, O, N, S), they are generally non-toxic, easy to recycle and their manufacturing is less energy-intensive than conventional inorganic electrodes.[3] Another aspect of interest of organic molecules applied to

[a] Dr. T. Lombardo,[+] F. Lambert,[+] R. Russo,[+] Dr. F. M. Zanotto, Dr. C. Frayret, Dr. M. Becuwe, Prof. Dr. A. A. Franco
Laboratoire de Réactivité et Chimie des Solides (LRCS), UMR CNRS 7314
Université de Picardie Jules Verne, Hub de l'Energie
15, rue Baudelocque, 80039 Amiens Cedex 1, France
E-mail: alejandro.franco@u-picardie.fr
[b] Dr. T. Lombardo,[+] F. Lambert,[+] R. Russo,[+] Dr. F. M. Zanotto, Dr. C. Frayret, Dr. G. Toussaint, Dr. P. Stevens, Dr. M. Becuwe, Prof. Dr. A. A. Franco
Réseau sur le Stockage Electrochimique de l'Energie (RS2E), FR CNRS 3459
Hub de l'Energie
15, rue Baudelocque, 80039 Amiens Cedex 1, France
[c] F. Lambert[+]
French Environment and Energy Management Agency (ADEME)
20, avenue du Grésillé- BP90406 49004 Angers Cedex 01 France
[d] R. Russo,[+] Dr. G. Toussaint, Dr. P. Stevens
Department Electric Equipment Laboratory (LME)
EDF R&D
Avenue des Renardières, 77818 Morêt-sur-Loing Cedex, France
[e] Dr. C. Frayret, Prof. Dr. A. A. Franco
ALISTORE-European Research Institute, FR CNRS 3104
Hub de l'Energie
15, rue Baudelocque, 80039 Amiens Cedex 1, France
[f] Prof. Dr. A. A. Franco
Institut Universitaire de France
103 boulevard Saint Michel, 75005 Paris, France
[+] These authors contributed equally to this article.

Supporting information for this article is available on the WWW under https://doi.org/10.1002/batt.202200116

battery electrodes is the possibility to modify (functionalize) their chemical structure according to the needs, enabling their potential, energy density, and cycle life to be tuned for example.[9,10] Their low cost, structural flexibility, and easier recycling are important assets for modern battery designs.[11] However, current organic-based electrodes still have several disadvantages: lower energy density than their inorganic counterpart, low electronic conductivity (except for conductive polymers), and low cycle life due to, among others, the material solubility in the electrolyte.[10,12] The latter, however, can also be seen as an advantage for redox-flow battery applications.[13]

In recent years, most of the research in the field has focused on identifying organic molecules suited for battery applications, mainly in the context of LIBs and sodium-ion batteries (SIBs). Among them, the most promising identified molecules are carbonyls (as quinone compounds), organodisulfides, azocompounds and nitriles for positive electrodes,[14–16] carboxylates and azobenzene for negative electrodes.[17] While the search for optimal organic materials is still far from over, in this work we do not focus on the materials chemistry, but rather on the electrode microstructure and its links with manufacturing and electrochemical performance, an aspect that is still understudied in the field of organic-based electrodes.

In our group, in the context of the ARTISTIC project,[18] we have previously developed a series of three-dimensional (3D) manufacturing models simulating the LIB slurries, their drying, the resulting electrode calendering, and the electrolyte filling,[19–24] which can be coupled to 4D (3D + time) electrochemical models accounting for galvanostatic (dis)charge[25,26] and electrochemical impedance spectroscopy.[27] All these models explicitly account for both the active material (AM) and carbon-binder domain (CBD) spatial location and their physics. The manufacturing models were validated by comparing macroscopic observables that can be measured experimentally and simulated computationally, like the slurry viscosity and density, or the electrode porosity. This computational workflow was initially developed and validated by considering commercial materials such as $LiNi_{0.33}Mn_{0.33}Co_{0.33}O_2$ (NMC) used as the reference AM. More details on these models, which are now also freely available through an online user-friendly interface,[30] can be found in Refs.[19–22,28] The main assumptions behind these models are the consideration of both the AM and CBD phases as spherical particles, accounting explicitly for the AM particle size distribution, and the non-consideration of the carbon and binder as separate entities, but rather their agglomerates, described by the CBD particles.

In the present work, we further tested these models, to verify their "chemistry neutrality", by applying them to organic-based electrodes, i.e., to an extremely different scenario compared to materials such as NMC: from inorganic to organic materials, from LIBs to SIBs, from commercial to in-house synthesized AMs, from N-methyl-2-pyrrolidone (NMP) based to water-based slurries, from high AM weight percentages, e.g., 95 wt.% for NMC, to a much lower one, i.e., 60 wt.%.

The organic molecule of choice for this study is the disodium biphenyl-4,4′-dicarboxylate (Na_2BPDC) salt, represented in Figure 1, which was first studied as a negative electrode by Choi et al.[29] for SIB applications, which can reversibly exchange two electrons through the carboxylic groups. Na_2BPDC electrodes exhibited promising electrochemical performance in half-cell configuration *vs* metallic sodium: they found a reversible specific capacity after the first cycle comparable to standard inorganic materials (200 mAh g^{-1}) with an average redox potential for sodium (de-)insertion at around 0.5 V vs. Na/Na^+.

Despite these interesting electrochemical properties, the formulation of the electrode by Choi et al. was not optimized, with a low AM weight ratio (ca. 57 wt.%) and loading (ca. 1 mg cm^{-2}), far from the standards required for the industrial applications. Therefore, studies focusing on the composite electrode formulation are needed and could make Na_2BPDC an excellent candidate to replace hard carbon (HC) as a negative electrode in full SIBs, especially for high power applications.

In the following, we first validate our 3D computational workflow in terms of reproducing the macroscopic properties (slurry density and viscosity, and electrode porosity) of the experimental Na_2BPDC slurry and electrode. Then, we analyze the ionic and electronic properties of the simulated electrodes to identify the best candidate for optimal electrochemical performance, which is then verified experimentally by a series of rate-capability tests in half-cell configuration. Lastly, the conclusions and perspectives of this work are drawn.

Results and Discussions

The main objective of this work is the application of 3D manufacturing models to Na_2BPDC-based anodes. Our manufacturing models account for three key steps of electrode manufacturing: the slurry phase, its drying, and electrode calendering. Each of these models requires as input two kinds of parameters, here referred to as manufacturing parameters and force field (FF) parameters, while its main output is the 3D slurry or electrode microstructure, which is later used as starting point for the next manufacturing model (drying after the slurry, calendering after the drying).

The manufacturing parameters are defined as the parameters linked to the experimental manufacturing: here the slurry solid content (SC), the slurry/electrode AM and CBD wt.%, the AM particle size distribution (PSD), and the electrode compres-

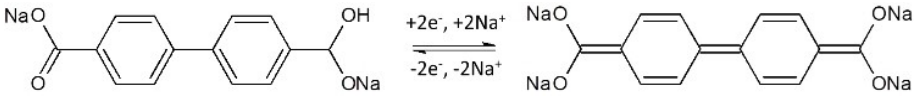

Figure 1. Disodium biphenyl-4,4′-dicarboxylate (Na_2BPDC) salt representation

sion during calendering. The FF parameters are internal parameters of the model, and they define the strength of interactions between AM and CBD particles. For the models presented here, the FFs of choice are the Lennard-Jones[30] (LJ) and Granular-Hertzian[31] (GH) FFs, mimicking particles attractive interactions and mechanical properties, respectively. The value of the FF parameters is unknown, and they should be tuned to fit the experimental observables taken as reference: in our case, the slurry density and shear-viscosity curve for the slurry phase, and the electrode porosity for the drying simulation. Figure 2 depicts a schematic of the computational workflow followed and the comparison of the aforementioned observables, demonstrating a good fit between experimental and simulated results.

Concerning the manufacturing parameters, most of them were kept constant in the simulations presented in this work, and their values were defined experimentally. In particular, here we utilized the "optimal" formulation in terms of AM and CBD wt.%, and SC (see the experimental section for details), where the "optimal" was defined as the experimental condition that led to the most homogeneous coating and promising electrochemical performance. The AM PSD is a function of the synthetic route adopted (experimental section), and it was analyzed through granulometry and utilized directly as an input of the model (Figure S1 in the supporting information). Lastly, the model is also able to account for the CBD nanoporosity, which was kept constant to 50%, as found experimentally.[32] However, to further validate our computational workflow, we kept one manufacturing parameter, the degree of electrode compression during calendering, as an extra degree of freedom. This was done to verify if the simulated microstructures were representative enough to offer qualitative or semi-quantitative indications on the optimal calendering procedure, where optimal here refers to the best galvanostatic performance in half-cell configuration.

The most straightforward way to verify computationally the impact of calendering on galvanostatic (dis)charge, would have been to perform 4D galvanostatic (dis)charge simulations using as input the 3D microstructures outputted by the manufacturing model, as we have already demonstrated for the case of NMC-based cathodes.[21,25,27] This procedure could be straightforwardly applied to the electrode microstructures simulated here, but, unfortunately, for the case of SIBs there is a lack of data in the literature for critical parameters that are needed for these electrochemical simulations, like the electrolyte properties, or the solid Na diffusion coefficient. Accurately measuring these properties can be non-trivial[26,33] and it was not possible to determine them precisely through in-house measurements. This lack of data calls for "model" experiments[34] characterizing accurately not only the properties of LIB materials but also of SIBs, for which only very few examples can be found in the literature.[35]

To circumvent this bottleneck, we defined a simple observable accounting for both the electronic and ionic properties of the simulated electrodes, for which the best compromise should be found for optimal electrochemical performance. The idea behind this approach is to use this observable as a qualitative indicator of the most suited calendering degree for optimal electrochemical performance. The parameters of choice for the electronic and ionic properties of the simulated electrodes were their effective electronic conductivity ($\delta_{electronic}$) and tortuosity factor (τ), respectively. $\delta_{electronic}$ was determined through GeoDict (Math 2 Market) accounting for the electronic conductivity of Na_2BPDC, which was measured through devoted *in-house* measurements (experimental section), and of CBD agglomerates[25] made of carbon black and binder. τ was

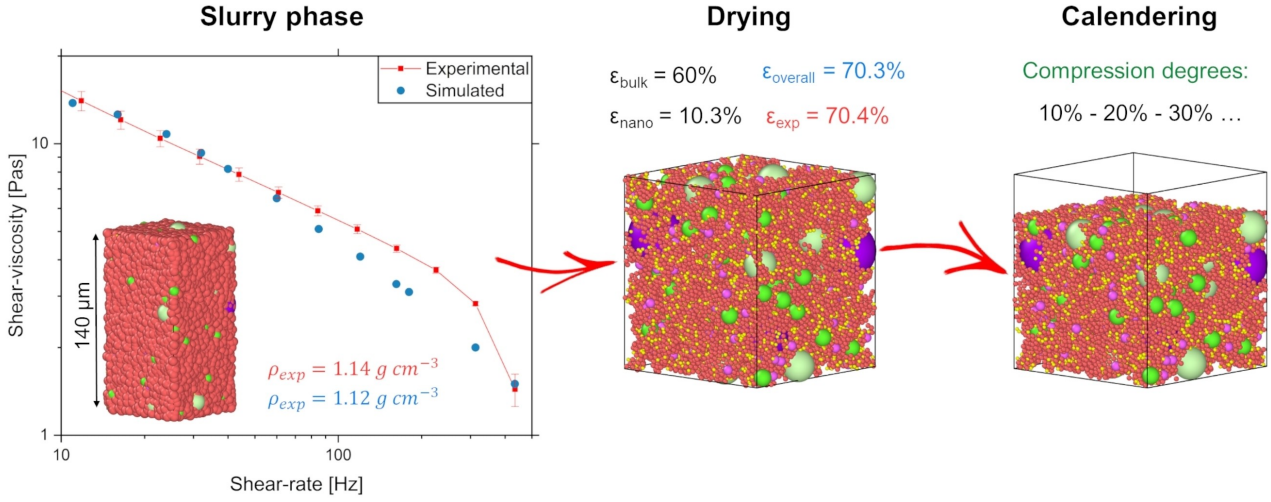

Figure 2. Schematic of the computational workflow followed in this work. First, the slurry phase is simulated, and its density and shear-viscosity curve are compared with their experimental counterparts, showing a good fit. Afterward, the slurry microstructure is used as input for the drying model, whose FF parameter values are adjusted to fit the experimental electrode porosity. The model can also distinguish between micro (ε_{bulk}) and nanopores (ε_{nano}), whose sum is the overall electrode porosity. Lastly, the dried electrode microstructure is used as input for the calendering simulation, consisting of compression of the electrode up to a set fraction of the initial thickness. Red particles stand for the CBD, while the remaining colors stand for the AM particles of different sizes (one for each color).

Research Article
doi.org/10.1002/batt.202200116
Chemistry Europe
European Chemical Societies Publishing

determined by approximating the electrolyte ionic diffusivity to be equal to the one of LP30, and accounting for the CBD nanoporosity.[21] Figure 3 depicts the normalized ratio of the electrode $\delta_{electronic}$ and τ, which should be maximized for improving the electrochemical performance. A maximum is observed at a high (50%) degree of compression. Compressing the electrodes for $>55\%$ of their thickness led to numerical instabilities of the simulation caused by too high forces acting on the particles, which is the reason why no result above this critical value is reported.

To validate this trend, four different calendering conditions (compression rates of 10%, 20%, 30%, and 50%) were selected and tested experimentally through rate capability tests in half-cell configuration (Figure 4). The discharge curves at C/10 (full lines) and 1C (dashed lines) for the 4 electrode compressions investigated are shown in Figure 4(a). The electrodes compressed at 10% and 20% showed similar discharge specific capacities (C/10 \ 1C) equal to 107 \ 14 mAh g^{-1} and 109 \ 3 mAh g^{-1}, respectively. A marked increase was observed for 30% compression, where the capacity rises to 126 \ 55 mAh g^{-1}; however, the highest specific capacity was observed for the electrode with 50% of compression, equal to 154 \ 95 mAh g^{-1}. An analogous trend can be observed for the charge curves. This result is also confirmed by the rate capability tests (C/10, C/5, C/2, and 1C) for different compressions. At each C-rate, the 50% compressed electrode exhibited the highest reversible specific discharge capacity, from 154 mAh g^{-1} at C/10 to 95 mAh g^{-1} at 1C, which corresponds to a retention of 60% of the capacity. Lower retentions were observed for the other electrodes tested, i.e., 43% for the electrode compressed at 30% of their thickness, while the discharge specific capacity of the 10% and 20% electrodes is reduced by half at C/2, and reduces to less than 15 mAh g^{-1} at 1C. Further information on the electrochemical performances observed for each compression and C-rates can be found in the supporting information (Figures S5 and S6). Overall, all these results indicate that the electrode with a compression rate of 50% is the one presenting the most advantageous electrochemical behavior at all the C-rates tested, in agreement with the computational results shown above. However, it was not possible to verify experimentally that going above a 50% compression degree leads to a decrease in performance, because it was not possible to compress the electrodes beyond 50% of their initial thickness with the calendering machine available to us. Although we cannot exclude that higher compressions can be attained by other means, this result is in good agreement with the impossibility of compressing the simulated electrode more than 55% of its initial thickness within the model, despite the not accounting for phenomena like particle cracking or deformation.

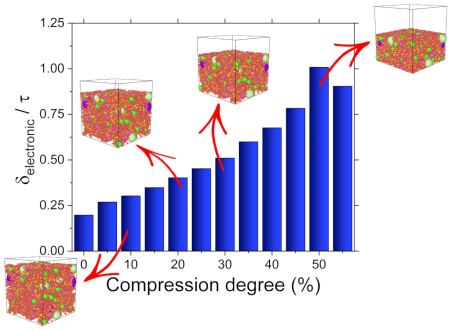

Figure 3. Normalized ratio of the electrode $\delta_{electronic}$ and τ as a function of the electrode degree of compression. The normalization is performed by dividing by the maximum. As a reference, a compression degree of 10% indicates an electrode that was compressed for 10% of its initial thickness during calendering. The 3D rendering of the simulated electrode microstructures associated with the conditions tested experimentally are illustrated explicitly (same color legend of Figure 2).

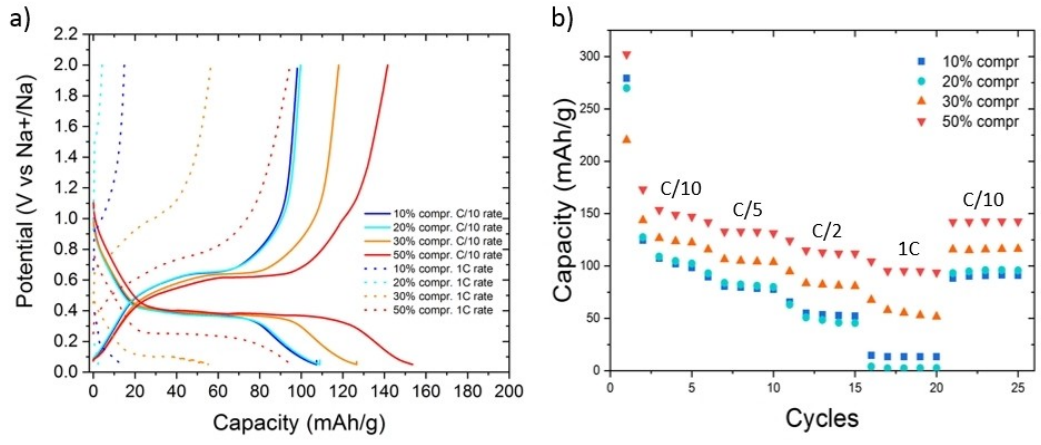

Figure 4. Galvanostatic performance for electrodes compressed at 10% (blue), 20% (light-blue), 30% (orange), and 50% (red) of their initial thickness for different C-rates (C/10, C/5, C/2, and 1C). a) Charge and discharge curves for the intermediate (3rd) cycle at C/10 (full lines) and 1C (dashed lines) for all the calendering conditions tested. b) Discharge specific capacity as a function of the cycle number for all the calendering conditions tested. All the results were obtained in half-cell configuration (coin cell) versus metallic Na, using $NaPF_6$ (1 M) in ethylene carbonate: dimethyl carbonate (volume ratio of 1:1) as electrolyte (150 µl), and a Whatman glass fiber separator. The electrodes surface was 1.3 cm^2, with an active loading in the range of 3.6–3.9 mg cm^{-2}, while the electrode thickness (no current collector) and porosity of the 10%, 20%, 30%, and 50% electrodes were ca. 100, 90, 75, 60 µm and *ca.* 67%, 64%, 59%, 30%, respectively.

Conclusion and Perspectives

This article presents the implementation of a 3D computational workflow simulating battery electrode manufacturing in the context of organic-based anodes using in-house synthetized Na_2BPDC as active material. Such a computational workflow accounts for the slurry phase, its drying, and electrode calendering, and was originally developed in the context of LIB electrode manufacturing, using inorganic AMs. In this work, we demonstrate that the same computational workflow can be utilized for a significantly different scenario: we moved from LIBs to SIBs, from inorganic to organic materials, from commercial to in-house synthesized AMs, from N-methyl-2-pyrrolidone (NMP) based to water-based slurries, from high AM weight percentages, e.g., 95 wt.% to a much lower one, i.e., 60 wt.% for Na_2BPDC.

The manufacturing simulations were validated by comparing the experimental and simulated slurry density, shear-viscosity curve, and the electrode porosity, for which a good fitting between experiments and simulations was shown. In addition, we utilized a qualitative observable, defined as the ratio between the electrode electronic conductivity and tortuosity factor, to characterize the electrode microstructures as a function of the calendering degree. The analysis of this observable indicated that optimal electrochemical performance should be obtained when compressing the electrodes to 50% of their initial thickness, suggesting that the electronic conductivity is the main limiting factor of the electrochemical performance of Na_2BPDC-based composite electrodes. In addition, the model showed a limit of compressibility of the electrode at approximately 55%. The validity of the aforementioned trends was tested experimentally through galvanostatic cycling in half-cell configurations for four different conditions: electrodes compressed at 10%, 20%, 30%, and 50% of their initial thickness. The experimental results showed that the electrode for which the compression rate is 50% behaves the best, and that further compression was not achievable through the calendering machine utilized, both confirming the trends identified computationally.

In terms of perspectives, this work is an important demonstration of the chemical neutrality of the ARTISTIC project manufacturing models, opening the door to their implementation to both inorganic and organic AMs. Furthermore, the same mixed (experimental + computational) procedure could be applied to study the impact of other manufacturing parameters and their combination, like identifying the optimal compression degree as a function of the electrode formulation of interest.

Computational Section

All the manufacturing simulations were performed using the open-source software LAMMPS. Approximately 25,000 particles were simulated (6,000 AM and 19,000 CBD). The size of the CBD particles in the dried and calendered electrode was of 2 μm, while it was expanded to account for carbon + binder + solvent at the slurry phase, as in Refs[19–22,28] . The AM sizes selected to account for the experimental Na_2BPDC particle size distribution were 1.5, 3.9, 6.95, 13.1, and 22.7 μm, whose frequency were calculated as weighted average of the experimental one (Figure S1). The system previous to the slurry simulation was initialized through generation of the AM and CBD particles in random position, as previously discussed by us.[19] All the FF parameter values used for the slurry, drying, and calendering simulations are reported in Table S1 and S2 of the supporting information. The slurry, drying, and calendering simulations took approximately 4, 3, and 0.25 days by using two nodes (128 GB of RAM) composed of 2 processors (Intel® Xeon® CPU E5-2680 v4 @ 2.40GHz, 14 cores) on the MatriCs platform (Université de Picardie-Jules Verne), respectively.

The effective electrical conductivity and ionic tortuosity factor of the electrode microstructures were calculated through the DiffuDict and ConductoDict modules of GeoDict (Math 2 Market). For the conductivity calculations, the Poisson equation is solved in the whole domain and then Ohm's law is used to obtain the effective electrical conductivity. The electronic conductivities of the AM and the CBD phases were set to $4.5\times10^{-5}\,S\,m^{-1}$ and $760\,S\,m^{-1}$, respectively. For the diffusivity calculation, Fick's first law is solved throughout the whole domain with a concentration difference Δc, and the effective Li^+ diffusivity is obtained from the overall diffusive flux j as: $d = -j \times \text{length}/\Delta c$. The diffusion coefficient within the pores was set at $7.5\times10^{-11}\,m\,s^{-2}$, while the diffusion within the CBD domain was calculated according to the Bruggeman relationships[27] ($D_{eff} = D_{bulk} \times \varepsilon^{1.5}$, where ε stands for the CBD nanoporosity, here 50%, and D_{bulk} and D_{eff} stand for the electrolyte diffusivity in the pore and in the CBD phases, respectively). The resulting value was equal to $2.6\times10^{-11}\,m\,s^{-2}$. The electrode tortuosity factor was calculated according to the McMullin number[36] ($N_M = \frac{\sigma_{bulk}}{\sigma_{eff}} = \frac{\tau}{\varepsilon}$, where σ_{bulk} and σ_{eff} are the bulk and effective ionic conductivities, τ the electrode tortuosity factor, and ε the electrode porosity). All of these input parameters were considered isotropic. Dirichlet boundary conditions were assumed for all external planes. For each of these properties, one value was computed for each Cartesian coordinate and their mean value was used to calculate the ratios between $\delta_{electronic}$ and τ as presented in Figure 3.

Experimental Section

The synthesis of Na_2BPDC was adapted from the lithium salt procedure reported by Choi *et al.*[29] 5.0 g of Biphenyl-4,4'-dicarboxylic acid (20.64 mmol) and 3 equivalent of sodium hydroxide (2.60 g, 61.92 mmol) were dissolved in 50 mL of methanol and stirred for 30 min; then, the solution was heated to 75 °C and stirred at reflux overnight. After 24 hours, the precipitate was retrieved by centrifugation and washed with methanol, acetone, and diethyl ether. The white solid was dried under vacuum at 120 °C for 8 hours. Yield: 91%. IR (cm^{-1}) selected bands: ν(O–C=O) 1578 (s), 1420 (s), 1394 (s), 775 (s) – Figure S7. 1H-NMR (D2O, 400 MHz, d ppm): 7.85 (d, 4H), 7.67 (d, 4H).

The composite slurry was prepared by mixing the active material with conductive carbon (Carbon Super C45) and binder carboxymethyl cellulose (CMC) in a mortar and then for 30 minutes using an Ultra-Turrax® tube drive (IKA, Germany) at 6000 rpm. The mass fraction of AM, carbon, and binder was 60 wt.%, 25 wt.%, and 15 wt.%, respectively. After that, water was added as a solvent (solid content of 24.5%) and mixed for 90 minutes at 4000 rpm. The shear-viscosity curve was acquired by applying a shear rate ramp (0.1–500 Hz) by using a rheometer (Kinexus lab+, Malvern Instruments), while the slurry density was measured through a density meter (DMA4500, Anton Paar GmbH). Both these properties were measured immediately after the slurry preparation. The

coating process was performed by a comma-gap machine (People & Technology Inc. model PDL-250) with two built-in ovens, each one of 1 m long. The temperature of both the two ovens was 60 °C. All the electrodes were coated over a 20 μm aluminum foil by fixing the comma gap and the line speed to 400 μm and 0.3 m min^{-1}, respectively. The calendering was performed through a prototype-grade lap press calender (BPN250, People & Technology, Korea), consisting of a two-roll compactor of 25 cm of diameter in which the gap between the rolls controls the pressure applied to the electrodes. The calendering was performed at various applied pressures, and at constant line speed (ca. 0.5 m min^{-1}) and roll temperature (60 °C).

Electrochemical impedance spectroscopy analysis was performed using the MTZ-35 frequency response analyzer (BioLogic, France). The sample was analyzed in the form of pellets: ca. 100–150 mg of Na_2BPDC powder were pressed using a 13 mm evacuable die set (Specac Ltd, UK) to obtain a homogenous pellet. The pellets' thicknesses were measured around 800 μm and with a diameter of 13 mm. The pellets were introduced into a controlled environment (CESH) sample holder to perform AC impedance measurements. All the steps of preparation were carried out in an Argon-filled glovebox ($0.1 < O_2$ ppm, $0.1 < H_2O$ ppm), to avoid the absorption of humidity by the sample. The impedance analysis was repeated at different stabilized temperatures, between 20 °C and 100 °C (on heating by 20 °C increments); the temperature was controlled through an intermediate temperature system (ITS) developed by Biologic, France. The measurements were performed in a frequency range of 3 MHz to 0.1 Hz (20 points per decade and 10 measurements per point), with an excitation voltage of 0.01 V. The electronic conductivities of the pellet were obtained from the Nyquist and Phase-Bode graphs of the complex impedance.

All the galvanostatic results were obtained by using coin cells (CR2032 type) in half-cell configuration versus metallic Na. The fiberglass separator (Whatman®) was soaked with 150 μL of an electrolyte made by 1 M $NaPF_6$ solution in ethylene carbonate: dimethyl carbonate with a volume ratio of 1:1 (all the solvents were certified battery purity grade, Merck). All cells were tested in a galvanostatic mode using a Biologic VMP-3 (Biologic SAS, France) instrument with a voltage window of 0.05–2.0 V. The cells were cycled at different C-rates, as C/10, C/5, C/2, and 1C (1C corresponds to 200 mA g^{-1}). The electrode surface was 1.3 cm^2, with an active material loading in the range of 3.6–3.9 mg cm^{-2} for all the samples, while the electrode thickness (no current collector) and porosity of the 10%, 20%, 30%, and 50% electrodes were *ca.* 100, 90, 75, 60 μm and *ca.* 67%, 64%, 59%, 30%, respectively.

Acknowledgements

A.A.F. and T.L. acknowledge the European Union's Horizon 2020 research and innovation program for the funding support through the European Research Council (grant agreement 772873, "ARTISTIC" project). A.A.F. and F.M.Z. acknowledges the European Union's Horizon 2020 research and innovation program under grant agreement No 957189 (BIG-MAP). T.L and R.R. acknowledge Charles Delacourt (LRCS, Amiens) for the useful discussions. F.L acknowledges the French Environment and Energy Management Agency (ADEME) and The European Regional Development Fund (FEDER) for supporting this work. All the authors acknowledge the MatriCS HPC platform from Université de Picardie-Jules Verne for the access to the computational resources utilized for the manufacturing simulations. RR is grateful to ANRT for partially supporting the funding of this research work between LRCS and EDF (Convention CIFRE N° 2019/0926). A.A.F. acknowledges the Institut Universitaire de France for the support.

Conflict of Interest

The authors declare no conflict of interest.

Data Availability Statement

The data that support the findings of this study are available from the corresponding author upon reasonable request.

Keywords: electrode · organic · manufacturing · microstructure · modeling · sodium-ion battery

[1] M. Armand, P. Axmann, D. Bresser, M. Copley, K. Edström, C. Ekberg, D. Guyomard, B. Lestriez, P. Novák, M. Petranikova, W. Porcher, S. Trabesinger, M. Wohlfahrt-Mehrens, H. Zhang, *J. Power Sources* **2020**, *479*, 228708.
[2] J. B. Goodenough, K. S. Park, *J. Am. Chem. Soc.* **2013**, *135*, 1167.
[3] P. Poizot, J. Gaubicher, S. Renault, L. Dubois, Y. Liang, Y. Yao, *Chem. Rev.* **2020**, *120*, 6490.
[4] S. Dühnen, J. Betz, M. Kolek, R. Schmuch, M. Winter, T. S. Placke Dühnen, J. Betz, M. Kolek, R. Schmuch, M. Winter, T. Placke, *Small Methods* **2020**, *4*, 2000039.
[5] IEA (2021), The Role of Critical Minerals in Clean Energy Transitions, IEA, Paris https://www.iea.org/reports/the-role-of-critical-minerals-in-clean-energy-transitions (Accessed on February 2022).
[6] IEA (2021), Global EV Outlook 2021, IEA, Paris https://www.iea.org/reports/global-ev-outlook-2021. (Accessed on February 2022).
[7] https://eur-lex.europa.eu/legal-content/EN/TXT/?uri=CELEX%3A02006L0066-20180704. Accessed on February 2022.
[8] P. Poizot, F. Dolhem, *Energy Environ. Sci.* **2011**, *4*, 2003.
[9] B. Esser, F. Dolhem, M. Becuwe, P. Poizot, A. Vlad, D. Brandell, *J. Power Sources* **2021**, *482*, 228814.
[10] Y. Liang, Y. Yao, *Joule* **2018**, *2*, 1690.
[11] S. Renault, D. Brandell, K. Edström, *ChemSusChem* **2014**, *7*, 2859.
[12] Z. Song, H. Zhou, *Energy Environ. Sci.* **2013**, *6*.
[13] J. Cao, J. Tian, J. Xu, Y. Wang, *Energy Fuels* **2020**, *34*, 13384.
[14] M. E. Bhosale, S. Chae, J. M. Kim, J. Y. Choi, *J. Mater. Chem. A* **2018**, *6*, 19885.
[15] B. Häupler, A. Wild, U. S. Schubert, B. Häupler, A. Wild, U. S. Schubert, *Adv. Energy Mater.* **2015**, *5*, 1402034.
[16] A. Mauger, C. Julien, A. Paolella, M. Armand, K. Zaghib, *Materials* **2019**, *12*, 1770.
[17] A. E. Lakraychi, F. Dolhem, A. Vlad, M. Becuwe, A. E. Lakraychi, A. Vlad, F. Dolhem, M. Becuwe, *Adv. Energy Mater.* **2021**, *11*, 2101562.
[18] https://www.erc-artistic.eu/ (Accessed on February 2022) .
[19] T. Lombardo, J. B. Hoock, E. N. Primo, A. C. Ngandjong, M. Duquesnoy, A. A. Franco, *Batteries & Supercaps* **2020**, *3*, 721.
[20] T. Lombardo, A. C. Ngandjong, A. Belhcen, A. A. Franco, *Energy Storage Mater.* **2021**, *43*, 337.
[21] A. C. Ngandjong, T. Lombardo, E. N. Primo, M. Chouchane, A. Shodiev, O. Arcelus, A. A. Franco, *J. Power Sources* **2021**, *485*, 229320.
[22] A. C. Ngandjong, A. Rucci, M. Maiza, G. Shukla, J. Vazquez-Arenas, A. A. Franco, *J. Phys. Chem. Lett.* **2017**, *8*, 5966.
[23] A. Shodiev, E. Primo, O. Arcelus, M. Chouchane, M. Osenberg, A. Hilger, I. Manke, J. Li, A. A. Franco, *Energy Storage Mater.* **2021**, *38*, 80.
[24] A. Shodiev, M. Duquesnoy, O. Arcelus, M. Chouchane, J. Li, A. A. Franco, *J. Power Sources* **2021**, *511*, 230384.
[25] M. Chouchane, A. Rucci, T. Lombardo, A. C. Ngandjong, A. A. Franco, *J. Power Sources* **2019**, *444*, 227285.
[26] M. Chouchane, E. N. Primo, A. A. Franco, *J. Phys. Chem. Lett.* **2020**, *11*, 2775.

[27] A. Shodiev, E. N. Primo, M. Chouchane, T. Lombardo, A. C. Ngandjong, A. Rucci, A. A. Franco, *J. Power Sources* **2020**, *454*, 227871.
[28] T. Lombardo, F. Caro, A. C. Ngandjong, J. B. Hoock, M. Duquesnoy, J. C. Delepine, A. Ponchelet, S. Doison, A. A. Franco, *Batteries & Supercaps* **2022**, *5*, e202100324.
[29] A. Choi, Y. K. Kim, T. K. Kim, M.-S. Kwon, K. T. Lee, H. R. Moon, *J. Mater. Chem. A* **2014**, *2*, 14986.
[30] https://lammps.sandia.gov/doc/pair_lj.html (Accessed in September 2021.
[31] https://lammps.sandia.gov/doc/pair_gran.html (Accessed in September 2021).
[32] L. Zielke, T. Hutzenlaub, D. R. Wheeler, C. W. Chao, I. Manke, A. Hilger, N. Paust, R. Zengerle, S. Thiele, *Adv. Energy Mater.* **2015**, *5*, 1401612.
[33] J. S. Horner, G. Whang, D. S. Ashby, I. V. Kolesnichenko, T. N. Lambert, B. S. Dunn, A. A. Talin, S. A. Roberts, *ACS Appl. Energ. Mater.* **2021**, *4*, 11460.
[34] S. Malifarge, B. Delobel, C. Delacourt, *J. Electrochem. Soc.* **2017**, *164*, A3925.
[35] D. Ledwoch, L. Komsiyska, E. M. Hammer, K. Smith, P. R. Shearing, D. J. L. Brett, E. Kendrick, *Electrochim. Acta* **2022**, *401*, 139481.
[36] R. B. MacMullin, G. A. Muccini, *AIChE J.* **1956**, *2*, 393.

Manuscript received: March 11, 2022
Revised manuscript received: March 25, 2022
Accepted manuscript online: March 29, 2022
Version of record online: April 19, 2022